Anisotropic macroturbulence and diffusion associated with a westward zonal jet: From laboratory to planetary atmospheres and oceans

Boris Galperin* and Jesse Hoemann
College of Marine Science, University of South Florida, St. Petersburg, Florida 33701, USA

Stefania Espa and Gabriella Di Nitto
DICEA, Sapienza Università di Roma, Via Eudossiana 18, 00184 Rome, Italy

Guglielmo Lacorata
ISAC, National Research Council, Strada Provinciale Lecce-Monteroni, 73100 Lecce, Italy
(Received 30 January 2014; revised manuscript received 27 July 2016; published 9 December 2016)

Turbulence with inverse energy cascade and its transport properties are investigated experimentally in a flow associated with a westward propagating jet. Turbulence and the jet were produced by an electromagnetic force in a rotating tank filled with an electrolytic saline solution. The parabolic free surface emulated the topographic β effect which evoked the zonation. The spectral and transport flow characteristics were highly anisotropic. Turbulence is diagnosed by exploring the analogy between vertical and horizontal turbulent overturns in, respectively, stably stratified and quasigeostrophic flows which gives rise to a method of potential vorticity (PV) monotonizing. The anisotropization of transport properties of the flow is investigated using the finite scale Lyapunov exponent technique. After initial exponential particle separation, radial (meridional in geophysical and planetary applications) diffusion attains a short-ranged Richardson regime which transitions to the Taylor (scale-independent diffusivity) one. The azimuthal (zonal) diffusion exhibits a double-plateau structure which attains a superdiffusive regime on large scales. The transition to the Taylor regime for the radial diffusion takes place at a scale of turbulence anisotropization. The radial eddy diffusivity in both regimes as well as the transition scale are all determined by the rate of the inverse energy cascade, ϵ, that can be diagnosed by the PV monotonizing. Conversely, ϵ can be deduced from the scale of the Richardson-Taylor regime transition in the radial eddy diffusivity which, thus, provides an additional tool of diagnosing anisotropic macroturbulence with inverse energy cascade.

DOI: 10.1103/PhysRevE.94.063102

I. INTRODUCTION

There has been a continuing interest in zonal (east-west) flows due to their importance for planetary atmospheric and oceanic circulations. Giant gas planets boast powerful zonal jets in both directions [1]; strong eastward jets dominate Earth's atmosphere and ocean's Antarctic Circumpolar and western boundary currents' extensions following their separations from the coasts [2], and narrower and weaker alternating jets or "striations" are observed in the oceans at midlatitudes [3–5]. The jets owe their existence to the restoring force associated with the latitudinal variation of the Coriolis parameter, $f = 2\Omega \sin\theta$, where Ω is the angular velocity of the planetary rotation, and θ is the latitude. A measure of this variation is $\beta = (1/R)df/d\theta = 2(\Omega/R)\cos\theta$, R being the planetary radius, and its impact is known as a β effect. The β-effect-related force is akin to an elastic force as it tends to return a displaced fluid particle to its equilibrium latitude giving rise to fluctuations around that latitude known as the Rossby waves. In summary, a fluid with a β effect is said to exhibit the *Rossby wave elasticity* [6].

Planetary circulations are usually concentrated in thin layers of large horizontal extent such that the horizontal velocities are much larger than their vertical counterparts. Although the flows are stably stratified, they feature large Reynolds numbers and are strongly nonlinear and turbulent. Due to the effects of geometric constraint, strong rotation and stable stratification, planetary fluids acquire properties of two-dimensional (2D) turbulence. In addition, planetary rotation and stable stratification facilitate material conservation of a new variable, the potential vorticity (PV) (e.g. [7]), which is intimately related to Rossby waves and controls many dynamic features. Rossby waves interact with planetary turbulence and, together, they form complicated wave-turbulence jigsaw puzzles [8] in which waves and turbulence coexist on all scales [9]. The union of turbulence and waves characteristic of large-scale planetary circulations can be thought of as *macroturbulence* [10].

The formation and maintenance of zonal jets can be related to the *horizontal* mixing of PV, in the same fashion as the formation and maintenance of layered structures in a stably stratified ocean can be related to the *vertical* mixing of the density gradient (e.g. [11,12]). While the former is a process that takes place on large scales and involves Rossby waves and turbulence with *up-scale* energy cascade, the latter occurs on relatively small scales and embroils the aggregation of internal gravity waves and turbulence characterized by a *down-scale* energy cascade.

Turbulent mixing in both cases is sustained by shear instabilities that draw their energy from external sources. The forcing renders the density and PV profiles nonmonotonic thus facilitating the instabilities. The power of the forcing that goes into turbulence in both cases can be estimated by

*bgalperin@usf.edu

 ©2016 American Physical Society

monotonizing the density and PV profiles using the Thorpe's sorting algorithm [13–15]. In the former case, this algorithm yields the Thorpe's scale, L_T, that was found commensurate with the Ozmidov length scale, $L_O = (\epsilon/N^3)^{1/2}$, where ϵ is the rate of the down-scale energy transfer and N is the Brunt-Väisälä frequency. Physically, L_O is a scale at which the turbulent eddy turnover time is equal to the period of internal gravity waves. The determination of L_T, which is often quite straightforward, is thus practically equivalent to estimating ϵ from L_O. In the latter case, the sorting algorithm yields a scale L_M that was found commensurate with the scale $L_\beta = (\epsilon/\beta^3)^{1/5}$ [16], where ϵ is the rate of the up-scale energy transfer [17–19]. In analogy to L_O, turbulence dominates the dynamics on scales shorter than L_β, while Rossby waves prevail on longer scales [20]. In practical situations, finding ϵ from L_M is much simpler and efficient than using the spectra that require extensive spatial and temporal data.

Macroturbulence entangles dynamics and transport and so some of the variables may be pertinent to both processes. By obtaining these variables from the dynamics, we may be able to learn about the transport and, vice versa, characteristics of turbulence may be amenable to diagnosis by analyzing transport and dispersion. One of the most important variables of such "dual use" is the rate of the energy transfer ϵ as it relates large-scale forcing to small-scale dissipation for flows with down-scale, or direct energy cascade, and small-scale forcing to large-scale dynamics for flows with up-scale, or inverse energy cascade. On the other hand, such crucial characteristics as eddy viscosities and eddy diffusivities are often related to either of ϵ dependent on the nature of a flow [21,22].

Generally, the external forcing (e.g. the solar heating) plays a paramount role in sustaining all planetary dynamic and transport phenomena and so our ability to estimate ϵ cannot be overstated. Numerous oceanographic and planetary observations indicate that the large-scale dispersion often obeys the Richardson's diffusion law at diverse locations and on a variety of scales [23–28]. Richardson's law involves ϵ and points to the underlying role of turbulence. The method of PV monotonizing can potentially be used for its estimation. The present study elaborates another method of diagnosing macroturbulence and estimating ϵ, this time by analyzing dispersion processes. The basic premise of this method is the observation detailed in [29] that in flows with dispersive waves and anisotropic inverse energy cascade, the meridional diffusion undergoes the transition from Richardson's to Taylor's diffusion regime. The scale of this transition is close to L_β, the fact that allows us to develop a new method which can be an alternative to PV monotonizing. When the data is sufficient to use PV monotonizing and dispersion estimate independently, the two methods provide a better constraint of the value of ϵ and allow us to avoid using data-intense spectral tools.

The analysis necessary for developing such diagnostics can be conveniently performed in a well-controlled environment of a laboratory facility. In our previous investigation, a facility at the University of Rome was used to explore the method of the PV monotonizing and quantify the relationship between L_M and L_β [16]. The present study extends this analysis to turbulent diffusion in a basic flow associated with a westward jet. Particle dispersion will be quantified by means of the finite-scale Lyapunov exponent (FSLE) method.

There are several reasons to concentrate the attention in the preceding and present studies on a westward jet despite the fact that major terrestrial oceanic and atmospheric jets are eastward. Physically, westward jets are prone to instabilities leading to PV mixing and eddy shedding (e.g. [30]). These features are common to the westward South-Equatorial currents in all oceans. Under the action of a seasonal forcing, these currents periodically become unstable and radiate waves known as the Tropical Instability Waves (TIWs) [31–33] and associated anticyclonic eddies to the north and south of the equator that play an important role in weather variability such as the El Niño–Southern Oscillation (ENSO) phenomenon (e.g. [34]).

Even more dramatic examples emerge from consideration of circulations of giant planets' atmospheres. Almost all westward jets on Jupiter and Saturn are barotropically unstable [35] and shed eddies of a variety of shapes, both cyclonic and anticyclonic. On Jupiter, a near 30°N westward jet irregularly undulates in latitude and is time variable in appearance, the features for which it was coined "The Jovian Ribbon" [36]. On Saturn, the 40°N westward jet becomes unstable on its southern flank and radiates trains of westward propagating cyclonic eddies sometimes referred to as the String of Pearls [37,38]. Many details of these phenomena are still unknown, either for the lack of data or understanding of physics, and our laboratory investigations are expected to provide new knowledge in both areas.

The paper is composed in the following manner. Section II describes the experimental setup, Sec. III provides the spectral analysis of the flow field, Sec. IV compares eddy diffusivities in quasigeostrophic and stably stratified turbulence and introduces the notion of the available rotational kinetic energy (ARKE) as a rotational counterpart of the available potential energy (APE), Sec. V discusses the FSLE method, Sec. VI applies this method to describe experimental results on diffusion, and Sec. VII is summary and conclusions.

II. EXPERIMENTAL SETUP

To study the method of PV monotonizing and associated diffusion laws, a series of laboratory experiments was performed in a tank filled with an electrolytic saline solution (mean depth of 4 cm) rotating counterclockwise (to emulate the Earth's rotation) with the angular velocity $\Omega = 3.0$ rad s^{-1}. The experimental facility is shown on Fig. 1. A detailed description of the facility is given in [39,40] where we studied anisotropic dynamic and transport processes in flows with a homogeneous forcing and their dependence on the flow parameters (i.e., the intensity of the forcing, rotation rate, etc.). The radius of the working section and the deformation radius were $R = 29.7$ cm and $L_D \simeq 10.4$ cm, respectively. The parabolic curvature of the free surface evoked a local β effect; the average value of β was about 0.53 $cm^{-1}\,s^{-1}$. The forcing was produced by passing a constant electric current through the working fluid over an array of 10 small, 12 mm in diameter, permanent magnets mounted under the bottom of the tank in a 90° arc of a radius $r = 17$ cm. The magnets were spaced at 1–2 cm from each other and had the same sense of polarity. This configuration induced a westward momentum

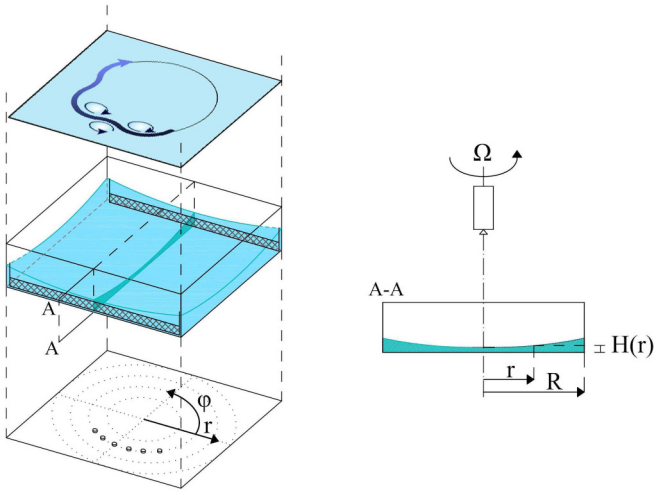

FIG. 1. Schematic representation of the experimental device. The magnets are placed in a 90° arc of the radius $a = 17$ cm (sector I).

that facilitated formation of a westward zonal jet. Unlike the meandering oceanic jets, sometimes referred to as striations, the stationary position of the magnets locked jet's location. The sector that contained the magnets was designated as sector I. The other three sectors were used for studies of the dynamics and diffusion in flows with inhomogeneous forcing and/or no direct forcing at all. The electromagnetic force also produced chaotic stirring whose scale, $L_\xi \simeq 1$ cm, was determined by magnets' diameter and spacing, both about 1 cm. This forcing sustained the inverse energy cascade.

Velocities were measured by analyzing images of passively advected styrene particles with mean size of about 5×10^{-5} m monitored by a video camera with a spatial resolution of 1023×1240 pixels at a frequency of 20 Hz. The particles were seeded at a fluid surface illuminated by two lamps. The contrast was enhanced by using white particles over a black bottom. The transparent lid of the tank insulated the working fluid from the ambient air. The camera corotated with the system and the data recording computer. The acquired images were analyzed by a feature tracking algorithm [39] that reconstructs particle trajectories from displacements between subsequent frames over a fixed time step of 0.05 s and produces instantaneous Lagrangian velocities. The time history of the Eulerian velocity field was then obtained by interpolating the sparse data over a regular grid. The polar coordinate grid employed in this study had $N = 60$ circles (radial resolution of about 0.5 cm) and $M = 90$ rays for each of the four sectors (angular resolution of 1°).

The Rossby number of the large-scale flow, $Ro = U/\Omega L$, U and L being typical velocity and horizontal scales, respectively, was reasonably small, $Ro = O(10^{-1})$, such that the flow could be analyzed in the framework of forced quasigeostrophic turbulence [41]. An important variable in this theory is the potential vorticity, q, given by

$$q = (\zeta + 2\Omega)/H(r), \tag{1}$$

where ζ is the vertical component of the relative vorticity and $H(r)$ is the fluid's depth. The variation of H with r produces a topographic γ effect which causes flow anisotropization and zonation, i.e., the formation and maintenance of zonal jets [42–44]. A local topographic β for experiments in a rotating tank was derived in [45].

TABLE I. Summary of the experimental setup and results.

Expt.	I[a] (A)	$10^4\epsilon$[b] (cm^2 s^{-3})	C_Z	n[c]	L_β[d] (cm)	U (cm s^{-1})	L_R[e] (cm)	R_β[f]
29	2	2.1	0.2	13	0.3	0.1	0.6	1
30	4	11.0	0.2	9	0.4	0.3	1.1	1.2
31	6	29.0	0.2	8	0.45	0.6	1.5	1.36

[a]Electric current.
[b]The rate of the inverse energy cascade.
[c]nth zero of the Bessel function with an index m, $J_m(\alpha_{mn}) = 0$.
[d]$L_\beta = (\epsilon/\beta^3)^{1/5}$.
[e]$L_R = (2U/\beta)^{1/2}$—the Rhines's scale.
[f]$R_\beta = L_R/L_\beta$—the zonostrophy index.

III. FLOW ANALYSIS

Three experiments, referred to as Exp. 29, 30, and 31, were performed. They only differed by the strength of the applied electric current, I, such that the rate of the energy injection due to the forcing was the sole controlling parameter. The values of I as well as the experimental results are summarized in Table I.

A. Visual appearance

The flow consisted of a westward (easterly) jet, large-scale eddies on both sides of it, and smaller-scale turbulence. Figure 2 shows instantaneous and time-averaged flow fields in sector I (90° sector on the right of the vertical line red in the color rendition) and sector II. The instantaneous images of sector I exhibit meandering jets squeezed between westward propagating eddies with the intensity of the eddies increasing with increasing forcing. The eddies were produced by the barotropic instability associated with the jet. On the one hand, the eddies highlighted the presence of the nonlinear Rossby waves, hence the direction of their propagation. On the other, they were maintained by the barotropic instability whose Rayleigh-Kuo (or Charney-Stern) threshold criterion is that the PV radial gradient, $\partial q/\partial r$, crosses the zero value. Accordingly, the zero crossings of the PV gradient were moving up and down (north and south, respectively) along any fixed radius thereby reflecting passing of the "northern" or "southern" (anticyclonic and cyclonic, respectively) eddies, respectively, as evident in Fig. 3. The dynamics of the interaction between zonal flows, Rossby waves, and eddies is very rich. Evidently, the large-scale eddies are produced by a combination of the small-scale forcing and the barotropic instability taking place on larger scales. The eddies give their energy back to a zonal flow thereby establishing a two-way energy exchange whose amplitude may exceed ϵ by several orders of magnitude. This result may seem paradoxical because, recalling the Riemann-Lebesgue theorem,

$$\lim_{k\to\infty} \int_0^1 f(x)\sin(kx)dx = 0$$

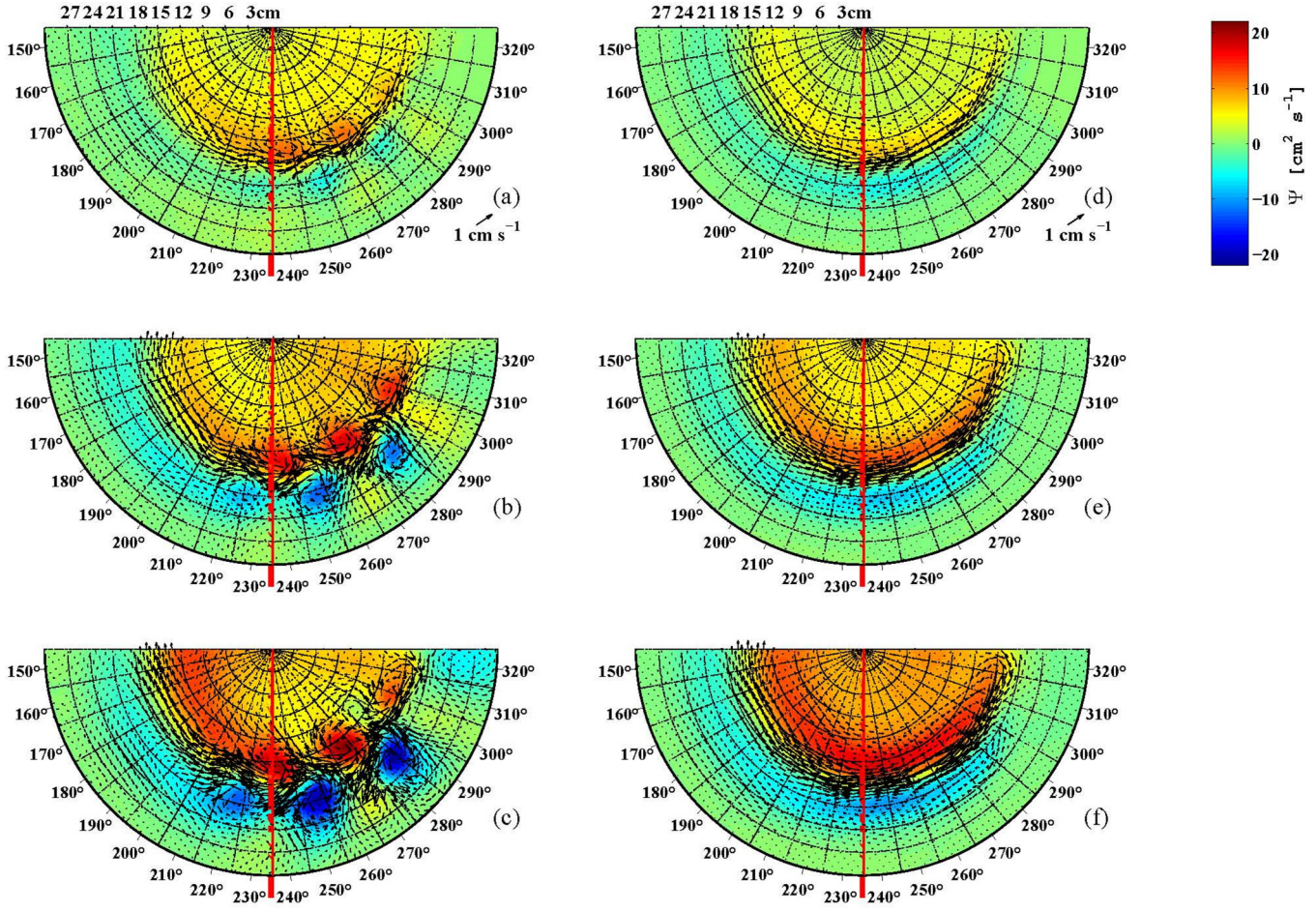

FIG. 2. Instantaneous [panels (a)–(c); experiments 29–31] and time-averaged [panels (d)–(f)] velocities and stream functions. The vertical line delineates the forced sector I located in the right halves of the semicircles.

for an $\mathbb{R}$-continuous function $f(x) : [0,1]$, one would expect that the long-term average of the amplitude of this exchange would tend to zero leaving no room for the effect of the small-scale forcing upon large-scale structures. This is not so, however, as Sukoriansky *et al.* [46] showed that such an average tends to ϵ thereby suggesting that the energy transfer oscillations are anharmonic.

In the unforced sector II, the eddies gradually die out after which one can only discern nonmeandering zonal jets. One infers that the system of eddies and meandering jet in sector I is sustained by direct local forcing. The time-averaged images present quite a different picture as they show strong alternating zonal jets and no eddies in all sectors. These experimental traits resemble ocean observations that highlight

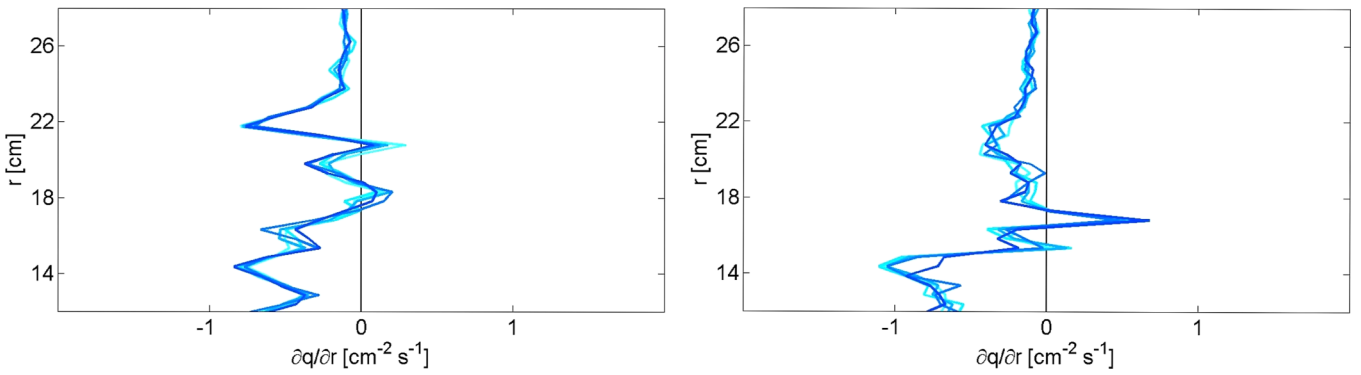

FIG. 3. Radial profiles of the instantaneous radial gradients of the potential vorticity, $\partial q/\partial r$, along the radial section at $\theta = 237^\circ$ for $t = 72$ s (left panel) and 95 s (right panel) for experiment 31. The five lines in each panel provide temporal representations. The dark line is the current instant, while the "older" lines (by only a frame or two) are shown in progressively lighter hue. This is done to ease the tracking of the movement of $\partial q/\partial r$.

numerous westward-propagating eddies closely entwined with zonal currents on relatively short time scales [5,47]. Upon time averaging, the meandering currents and eddies fuse into alternating zonal jets [4]. In analogy to other experiments (e.g. [48,49]), the scales of the eddies and jets exceed the forcing scales thus pointing to a complex interaction between the inverse energy cascade and eddies–zonal flows exchange.

B. Spectral analysis

Spectral analysis of the experimental results was performed using the truncated Bessel-Fourier decomposition in a 90° sector,

$$f(r,\phi) = \sum_{m=0}^{M}\sum_{n=1}^{N} J_m\left(\alpha_{mn}\frac{r}{R}\right)(a_{mn}\sin 4m\phi + b_{mn}\cos 4m\phi), \quad (2)$$

where $f(r,\phi)$ is an arbitrary well-behaving function such that $f(R,\phi)=0$, J_m is the Bessel function of the mth order, α_{mn} is its nth zero, and a_{mn}, b_{mn} are the expansion coefficients [50]. With the azimuthal resolution of 1°, M is limited to 45.

The argument of the Bessel function in (2) maps the space of geometric scales associated with the index n onto a space of scales associated with the Bessel functions' zeros, α_{mn}, for every index m. To restore a geometric scale corresponding to n from a scale associated with α_{mn} for a given m, one needs to multiply the latter by a factor α_{mn}/n.

To accommodate the spectral anisotropy due to a β effect, we define the zonal (radial) and residual spectra as, respectively,

$$E_Z(\alpha_{0n}) \equiv \frac{1}{2}b_{0n}^2 J_1^2(\alpha_{0n}), \quad (3)$$

$$E_R(\alpha_{mn}) \equiv \frac{1}{4}\sum_{m=1}^{M}\left(a_{mn}^2 + b_{mn}^2\right)J_{m+1}^2(\alpha_{mn}). \quad (4)$$

If and when a flow features inverse energy transfer and otherwise approaches the regime of zonostrophic turbulence [9,16], the spectra are expected to become

$$E_Z(\alpha_{0n}) \simeq C_Z\beta^2(\alpha_{0n}/R)^{-5}R^{-1}, \quad (5)$$

$$E_R(\alpha_{mn}) \simeq C_K\epsilon^{2/3}(\alpha_{1n}/R)^{-5/3}R^{-1}, \quad (6)$$

where $C_Z \simeq 0.5$, $C_K \simeq 6$. Two details need to be elaborated. First, since α_{mn}, m, and n are nondimensional numbers rather than wave numbers, the spectra represent the energy per unit number rather than unit wave number and so the expressions in the right-hand side (RHS) of (5) and (6) are divided by R to preserve correct dimensionality. Secondly, for relatively small n, only the first few nonzonal modes contribute to E_R significantly and so Eq. (6) contains α_{1n} only. The residual spectrum is approximated by the modes with $m=1$ that carry the maximum energy.

The zonal (5) and residual (6) spectra intersect at a scale

$$\hat{L}_\beta^0 \equiv R/\alpha_{0n} = (C_K/C_Z)^{3/10}(\alpha_{0n}/\alpha_{1n})^{1/2}L_\beta, \quad (7)$$

which defines the index n of the intersection. We note that $\hat{L}_\beta^0$ depends on the constants C_K and C_Z, while L_β is constant independent and, thus, better suited for the purposes of this study. We also note that such a defined scale corresponds to the index α_{0n}. As mentioned earlier, a corresponding geometric scale for $\hat{L}_\beta^0$ is obtained by multiplying (7) by a factor α_{0n}/n giving

$$\hat{L}_\beta = (\alpha_{0n}/n)\hat{L}_\beta^0 = R/n = (C_K/C_Z)^{3/10}(\alpha_{0n}/n)(\alpha_{0n}/\alpha_{1n})^{1/2}L_\beta. \quad (8)$$

This scale is the exact polar coordinate analog of the scale L_β used in, e.g. [9].

The relationship between $\hat{L}_\beta$ and L_β expressed by (8) is specific to the polar coordinate system due to the mapping of the space of n onto the space of α_{mn}. In other often used coordinate systems, i.e., Cartesian and spherical, such mapping is not required and so the proportionality coefficient between $\hat{L}_\beta$ and L_β is much simpler (e.g. [9]).

Figure 4 presents the spectra for all experiments and their rms fitting to expressions (5) and (6) [51]. The ranges of the available wave numbers are short yet marginally sufficient to determine the slopes. Figure 4 reveals strong anisotropy, whereas the zonal spectrum is steep and close to the -5 slope reminiscent of the regime of zonostrophic turbulence [9], while the residual spectrum is close to the Kolmogorov-Kraichnan (KK) law (6). The corresponding values of ϵ are given in Table I.

The presence of the $-5/3$ slope is insufficient to ascertain the existence of the inverse energy cascade as the direction of the energy flux cannot be deduced from a spectrum. It can be diagnosed independently by the analysis employing third order longitudinal structure functions, $D_{LLL} = \langle(\delta u_L)^3\rangle$, where δu_L is the velocity increment between two points projected onto a vector connecting these points, its length being ℓ, and $\langle\rangle$ denotes statistical averaging (e.g. [52–56]). In a locally isotropic and homogeneous turbulence, the structure functions are equal to

$$D_{LLL} = -4/5\epsilon\ell \quad (9)$$

for the direct energy cascade in 3D turbulence (the Kolmogorov four-fifths law) and

$$D_{LLL} = -3/2\epsilon\ell \quad (10)$$

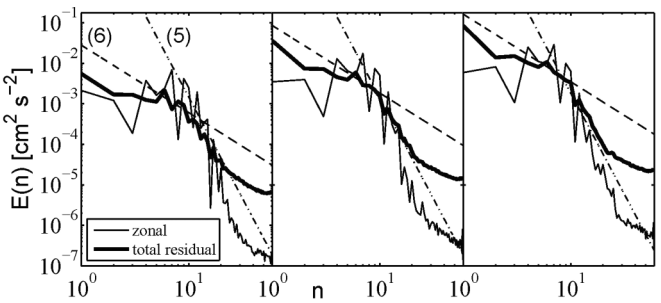

FIG. 4. Experimental zonal (E_Z, thin line) and residual (E_R, thick line) spectra and their rms fittings to Eqs. (5) and (6). The index n denotes the nth zero of the Bessel function with an index m, $J_m(\alpha_{mn})=0$, as explained after Eq. (2). Left, middle, and right panels pertain to the experiments 29, 30, and 31, respectively.

in 2D turbulence with inverse energy cascade. In the former case, $\epsilon > 0$ is the rate of the viscous dissipation, while in the latter, $\epsilon < 0$ is the rate of the inverse energy cascade. Thus the sign of D_{LLL} points to the direction of the energy flux—for the direct cascade, $D_{LLL} < 0$, while for its inverse counterpart, $D_{LLL} > 0$ [53,57,58].

Although the flows in the experiment are inhomogeneous and anisotropic, the time-averaged fields, as evident in Figs. 2(d)–2(f), may be assumed approximately axially symmetric if the structure functions are computed in the forced sector. The accuracy of this assumption increases with decreasing ℓ (e.g. [59]). Thus the sign of D_{LLL} provides the diagnostic of the direction of the energy cascade. With regard to the magnitude of ϵ, we keep in mind that Table I provides sector-averaged values which may be smaller than those obtained from the structure function analysis that produces localized values. Therefore, only an order of magnitude agreement can be expected.

The structure functions for all three experiments are shown in Fig. 5. They are positive for all experiments and for all ℓ, thus indicating that the flows indeed featured inverse energy cascade. The existence of the inverse cascade can also be inferred visually, from the disparity between small scales of the forcing and large scales of the resulting structures under the action of rotation with small Ro. For very small separations, $D_{LLL} \propto \ell^5$ for experiments 30 and 31, in agreement with Lindborg [53]. All structure functions exhibit a short linear regime starting at about 2.5 cm, 3.8 cm, and 4.5 cm and ending at about 3.5 cm, 6 cm, and 7.3 cm for experiments 29, 30, and 31, respectively. All these values approximately correspond to the beginnings and ends of the KK ranges in the spectra shown in Fig. 4. The lengths of the linear intervals are, approximately, 1 cm, 2.2 cm, and 2.8 cm, respectively. In

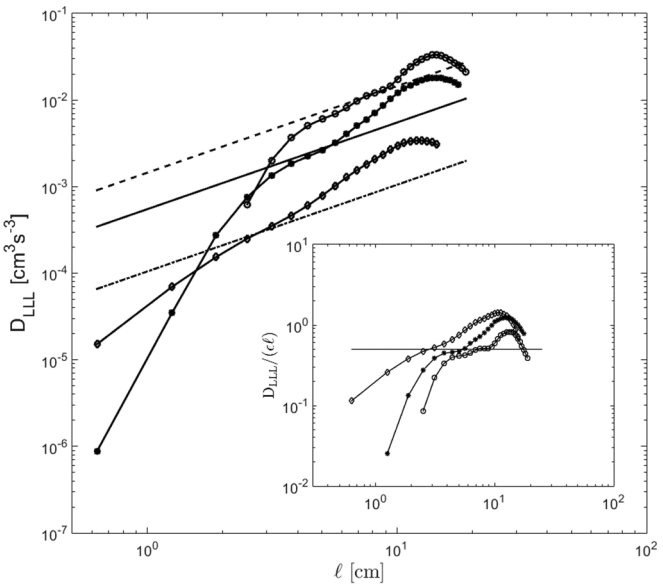

FIG. 5. Longitudinal structure functions for experiments 29 (lower line), 30 (middle line), and 31 (upper line). Normalized structure functions, $D_{LLL}/\epsilon\ell$, are shown in the inset with the order of the lines reversed and the horizontal line corresponding to $D_{LLL}/\epsilon\ell = 0.5$; ϵ is obtained from Table I.

the linear range, $D_{LLL} \simeq 0.5\epsilon\ell$ with the absolute value of ϵ estimated from the spectra and given in Table I. As mentioned earlier, only an order of magnitude agreement of D_{LLL} with Eq. (10) was expected.

In quasi-2D turbulence with inverse energy cascade and a β effect, possible flow regimes can be classified in terms of several nondimensional parameters formed by the ratios of characteristic length scales, L_ξ, L_D, L_β, and L_R, the latter being the Rhines scale, $L_R = (2U/\beta)^{1/2}$, where U is the rms of total velocity [60,61]. Since the deformation radius, L_D, was larger than the span of the jets and the eddies for all experiments, the zonation was unimpeded by the flow divergence (see, e.g. [62]) and so the dynamic effect of L_D was negligible. The two remaining relevant parameters are the zonostrophy index, $R_\beta = L_R/L_\beta$, and $R_\xi = L_\beta/L_\xi$. As shown in [9], the effect of the forcing scale becomes small for $R_\xi \gtrsim 2$. Although in our experiments R_ξ was smaller than 1, the forcing scale did not appear to make a significant impact.

The results of the spectral analysis are summarized in Table I. We note the relatively low values of the zonostrophy index R_β, between 1 and 1.36. As elaborated in [9,44], flows with $R_\beta \lesssim 2$ are eddy-dominated and feature weak [or latent (see, e.g. [63,64])] zonal jets. For comparison, the large-scale oceanic circulation, for which $R_\beta < 2$ [44], exhibits multiple westward propagating eddies (e.g. [47,65]) and latent zonal jets (e.g. [3,66]). As mentioned earlier in Sec. III A, similar to Fig. 2, the oceanic jets also become more distinct upon time averaging (e.g. [63,64,66]).

According to Table I, the coefficient C_Z in the zonal spectrum (5) is nearly constant for all experiments, $C_Z \simeq 0.2$. This value is in a reasonable agreement with the results of numerical simulations in [19] (about 0.4) but somewhat smaller than about 0.5 found in [60]. The near-constancy of C_Z, along with the very existence of the interval with the -5 slope for the zonal spectrum, could be construed as an evidence of the regime of zonostrophic turbulence. Given the low values of R_β, however, the presence of this regime is unexpected.

To understand the reason behind attaining near-zonostrophic spectra in the observed flow which was far from the zonostrophic regime, recall that in our previous numerical studies where zonostrophic regime was achieved, the forcing was homogeneous, isotropic, and concentrated on small scales (e.g. [9,67]). In the present experiments, however, the forcing was spatially inhomogeneous and the zonal jet was produced by direct application of the electromagnetic force, thus bypassing the zonation process. Most likely, this forcing facilitated the zonal kinetic energy spectra to attend distributions close to those in the zonostrophic regime. The zonal spectrum (5) is forcing independent and determined solely by β and the wave number, but the constant C_Z may be a function of R_ξ. It is possible that the spectrum (5) could be attained in forced β-plane turbulence with any forcing, forcing's properties determining the value of C_Z. If this indeed is the case, then laboratory flows analogous to those produced in the present experiments could be used as a proxy to the regime of zonostrophic turbulence.

Turning to the residual spectra we note that the indexes where $E_Z(n)$ and $E_R(n)$ intersect are in agreement with Eq. (8). The corresponding scale, $\hat{L}_\beta$, marks the threshold of spectral anisotropy. An analogous length scale in the spherical

geometry was identified in simulations in [60]. As evident from (8), although scales $\hat{L}_\beta$ and L_β are proportional, only the scale L_β is constant independent and thus better suited for the use in PV monotonizing algorithm [16]. The scale $\hat{L}_\beta$, on the other hand, plays an important role in characterization of diffusion processes [29]. Furthermore, as shown in the next section, it can be deduced from the observed diffusion characteristics thereby providing an additional to L_M tool of diagnosing macroturbulence.

IV. PARALLELS BETWEEN AVAILABLE POTENTIAL AND ROTATIONAL KINETIC ENERGIES AND BETWEEN EDDY DIFFUSIVITIES IN STABLY STRATIFIED AND QUASIGEOSTROPHIC TURBULENCE

In theories of homogeneous isotropic turbulence, it is customary to invoke a one-dimensional representation of the eddy diffusivity coefficient K [68],

$$K \propto \overline{u^2} T_L, \tag{11}$$

where $\overline{u^2}$ is a measure of the turbulence kinetic energy and T_L is the Lagrangian integral time scale. Conditions under which (11) can be recast in terms of the mixing length ℓ,

$$K \propto \overline{u^2}^{1/2} \ell, \tag{12}$$

were discussed in [24].

Geophysical and planetary turbulence is strongly anisotropic and so, if (12) were to be used, one needs to reassess the physical meaning of the mixing length ℓ in diapycnal and isopycnal applications. In both cases, models of K usually involve a product of an eddy velocity and an eddy length scale (e.g. [24,69,70] for the former and e.g. [71–77] for the latter) whose determination is a key unresolved problem.

In the spirit of the seminal work by Richardson [78] and following [9,29], we define $K(\ell)$ as an *effective* diffusivity accumulated at a scale ℓ due to contributions from all scales up to ℓ,

$$K(\ell) \propto \mathcal{E}(\ell)^{1/2} \ell, \tag{13}$$

where $\mathcal{E}(\ell)$ is the turbulence energy contained in all scales bounded by ℓ. For homogeneous isotropic turbulence with the Kolmogorov energy spectrum, Eq. (13) gives the classical Richardson diffusion law,

$$K(\ell) \propto \epsilon^{1/3} \ell^{4/3}, \tag{14}$$

where ϵ is the rate of either the direct or inverse energy cascade. The definition (13) can be expanded to anisotropic flows that combine turbulence and waves. The effect of the anisotropy is then reflected in the choice of ℓ in different directions.

A critical parameter in such flows is a scale at which a wave period is approximately equal to the time scale of turbulent overturns. Recall that in stably stratified flows, this is the Ozmidov scale, L_O, and in small-scale forced quasigeostrophic turbulence, such scale is L_β. Additional critical scales are those marking the respective thresholds of spectral anisotropy. They correspond to crossovers between the Kolmogorov and steep spectra developing in slow manifolds in the directions along which waves do not propagate [16,79]. Those scales are proportional to, respectively, L_O and L_β and denoted $\hat{L}_O$ and $\hat{L}_\beta$. Simulations (e.g. [29]) and experiments (e.g. [39]) indicate that along these directions, only the scales up to $\hat{L}_O$ or $\hat{L}_\beta$ contribute to the eddy diffusivity. On larger scales, ℓ remains "frozen" at the $\hat{L}_O$ or $\hat{L}_\beta$ values and so $K(\ell)$ becomes scale-independent and reminiscent of the Taylor regime. In the orthogonal directions, however, diffusion obeys the Richardson law on much longer scales until overtaken by the zonal advection, particles' trajectories decorrelation, etc.

In the case of stable stratification, $\mathcal{E}(\ell)$ in the Taylor regime is $\mathcal{E}(\ell) = \mathcal{E}(\hat{L}_O) = \frac{1}{2} N^2 \hat{L}_O^2 \equiv E_p$, where E_p is the part of the *available potential energy* (APE) that can be converted to turbulence (note that $E_p \to 0$ when $\epsilon \to 0$). The vertical eddy diffusivity in this case,

$$K_z(\hat{L}_O) \propto E_p^{1/2} \hat{L}_O \propto \frac{\epsilon}{N^2}, \tag{15}$$

is the celebrated Ellison-Britter-Osborn expression.

Since $\hat{L}_O \simeq L_T$ [15], density monotonizing yields the value of ϵ and thus the vertical and horizontal eddy diffusivities in both Richardson and Taylor regimes [21,79].

A similar analysis can be performed on (13) for quasigeostrophic turbulence where the appropriate scale is $\hat{L}_\beta$ and the kinetic energy of turbulence can be computed from the KK spectrum which usually exists on scales not exceeding $\hat{L}_\beta$,

$$E_r = \int_\infty^{\hat{n}_\beta} C_K \epsilon^{2/3} n^{-5/3} dn = \frac{3}{2} C_K \epsilon^{2/3} \hat{n}_\beta^{-2/3}. \tag{16}$$

Here, $C_K \simeq 6$ is the Kolmogorov-Kraichnan constant and $\hat{n}_\beta$ is the wave number corresponding to the scale $\hat{L}_\beta$. In the spherical geometry, $\beta = \Omega/R$, where Ω and R are, respectively, the angular velocity and the radius of a sphere [60]. Introducing a nondimensional index $\tilde{n}_\beta = R\hat{n}_\beta = \pi R/\hat{L}_\beta$, Eq. (16) can be transformed to

$$E_r = (3/2) C_K \Omega^2 R^2 \tilde{n}_\beta^{-4}. \tag{17}$$

In analogy to E_p, E_r defines a part of the *available rotational kinetic energy* (ARKE) in quasigeostrophic flows that can be converted to turbulence ($E_r \to 0$ when $\epsilon \to 0$). Since the rotational kinetic energy (per unit mass) of a solid body with the moment of inertia I rotating with the angular velocity Ω is $\frac{1}{2} I \Omega^2$, the product $3 C_K R^2 \tilde{n}_\beta^{-4}$ plays a role of the equivalent moment of inertia of a flow on scales dominated by turbulence.

On a fast rotating sphere, in the regime of zonostrophic turbulence, the total rotational kinetic energy of a flow, including the zonal jets, can be approximated by

$$E_t \simeq (5/4) C_Z \Omega^2 R^2 \tilde{n}_R^{-4}, \tag{18}$$

where $C_Z = O(1)$ and $\tilde{n}_R$ is the index associated with the Rhines scale $L_R = (2U/\beta)^{1/2}$, with U being the rms of total velocity [61,80] [in (18) we take into account that the part of the spectrum for $n \leqslant n_R \propto L_R^{-1}$ may be flat due to the action of a large-scale drag]. As in Eq. (16), one can identify the product, $(5/2) C_Z R^2 \tilde{n}_R^{-4}$, with the equivalent moment of inertia of the total flow. Note that while E_r substantially depends on ϵ, E_t depends on a single geometrical property of the zonal jets, their width which roughly scales with L_R [61].

Viewed as a measure of the zonal jets' variability due to turbulence, the ratio E_t/E_r can be expressed in terms of the

zonostrophy index $R_\beta \equiv \tilde{n}_\beta/\tilde{n}_R$,

$$\frac{E_t}{E_r} \simeq \frac{5C_Z}{6C_K}\left(\frac{\tilde{n}_\beta}{\tilde{n}_R}\right)^4 = \frac{5C_Z}{6C_K}R_\beta^4, \tag{19}$$

which rapidly increases with R_β. In the ocean, where $R_\beta \simeq 1.7$ [44], the ratio (19) is $O(10^{-1})$ and the jets are hardly distinguishable from turbulence, i.e., latent. On Jupiter, on the other hand, $R_\beta \gtrsim 5$ [28], the ratio (19) is $O(10^2)$ and so the zonation is profound, the zonal jets are strong, and the turbulence signal is weak, just as observed on Jupiter and Saturn.

By analogy with (15), substituting $E_r^{1/2}$ and $\hat{L}_\beta$ in (12) one obtains an expression for the scale-independent, Taylor-regime-like lateral eddy diffusivity in forced quasigeostrophic turbulence,

$$K_y(L_\beta) \propto E_r^{1/2}\hat{L}_\beta \propto \epsilon^{3/5}\beta^{-4/5}, \tag{20}$$

with an $O(1)$ coefficient. This scaling was verified in laboratory experiments [39].

The Taylor-like eddy diffusivities for the vertical and meridional mixing, Eqs. (15) and (20), respectively, in anisotropic turbulence with dispersive waves constitute profound physical laws with important practical implications.

For the former, consider vertical (diapycnal) mixing in the Antarctic Circumpolar Current (ACC). In the framework of the DIMES (Diapycnal and Isopycnal Mixing Experiment in the Southern Ocean) campaign, Ledwell *et al.* [81] studied vertical diffusion of trifluoromethyl sulfur pentafluoride (CF_3SF_5) released at the isopycnal surface of about 1500 m at the latitude of the release. The vertical spread of the tracer was observed for 1 yr and the final profile was compared with the one computed using a one-dimensional diffusion equation with a constant, Taylor-like diffusivity coefficient, $K_z = 1.28 \times 10^{-5}$ m^2 s^{-1}, best fitted to the evolution of the mean profile. The result of this comparison is shown in Fig. 6. The tracer spread nearly equally, for about 100 m, up and down from the release height with no accumulation at any particular level, i.e., no level exhibits features of a mixing barrier. The measure of turbulent overturns, the Ozmidov scale L_O, was only about 1 m, which is considerably smaller than the vertical size of the tracer's spread. This result indicates that the actual mixing was taking place everywhere in the tracer's cloud on scales of the order of L_O and the total spread was a cumulative effect of a large number of small-scale overturning mixing events. With the measured value of the Brunt-Väisälä frequency, $N \simeq 1.5 \times 10^{-3}$ s^{-1}, the Ellison-Britter-Osborn model (15) with the proportionality coefficient set at 0.2 was utilized to estimate the rate of the viscous dissipation, ϵ, from the value of K_z. Thus obtained value of ϵ was about 50% higher than the estimate based on direct measurements using the microstructure profiler.

With regard to the meridional diffusivity in the environment of turbulent flows with inverse cascade, we use Eq. (20) to describe the lateral spread of the debris and gases after the Shoemaker-Levy 9 (SL9) comet impact upon Jupiter in 1994 (see, e.g. [82]). The debris and gases turned out to be natural conservative tracers perfectly suited for dispersion observations. Such observations were conducted for several years following the impact.

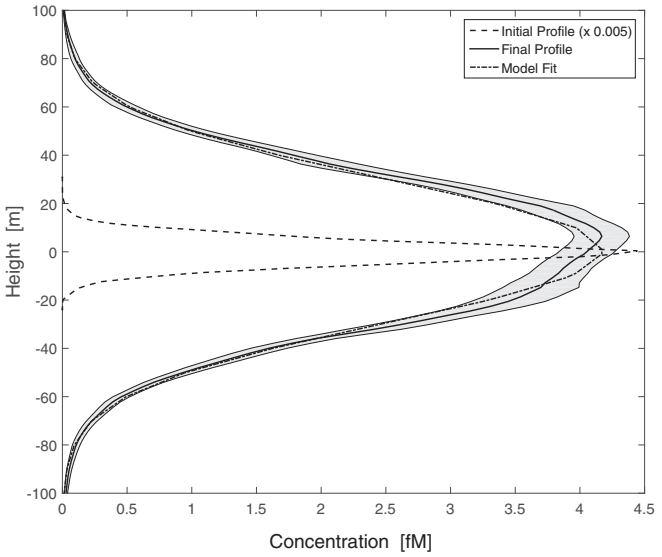

FIG. 6. Vertical diffusion of a tracer in the Antarctic Circumpolar Current. The ordinate is height relative to the center of the initial profile. The abscissa is the concentration in femtomolars (fM; 1 fM = 1×10^{-15} moles/liter). Dashed curve: initial mean concentration measured shortly after release, multiplied by 0.005. Solid curve: final mean profile measured 1 yr later. The gray uncertainty envelope is based on variations of the shape of individual profiles. Dash-dotted curve shows final profile for an integration of the one-dimensional diffusion equation, starting with the initial profile, for a diapycnal diffusivity of 1.28×10^{-5} m^{2}s^{-1}. After Ledwell *et al.* [81]. ©American Meteorological Society. Used with permission.

A study by Friedson *et al.* [27], in which mean optical depth was used as a concentration surrogate, concluded that the advection due to the residual circulation was insufficient to describe the temporal dispersion of the impact cloud and so the authors included meridional diffusion with a scale-independent, Taylor-type diffusivity coefficient, $K_y = (1-10) \times 10^6$ m^{2}s^{-1}, in the region between 10 and 100 mbar. Our estimate based upon Eq. (20), with the rate of the inverse energy cascade $\epsilon \simeq 10^{-5}$ m^{2}s^{-3}, as estimated from the Cassini data by Galperin *et al.* [28], and $\beta \simeq 10^{-12}$ m^{-1}s^{-1}, yields $K_y \simeq 4 \times 10^6$ m^{2}s^{-1}, in good agreement with the values used in [27]. In addition, unlike calculations in the latter paper, Eq. (20) produces no negative eddy diffusivities.

Figure 7 shows the meridional spread of the cloud of debris as a function of time. A gradual meridional expansion of the initially latitudinally narrow tracer profile is evident, just as it was in the case of the vertical diffusion in the ACC discussed earlier. As in the ACC case, the maximum size of eddies contributing to K_y was L_β, a scale approximately R_β ($R_\beta \simeq 5$) times smaller than the width of a zonal jet. This scale was considerably smaller than a scale of the lateral expansion of the debris cloud yet there was no debris accumulation at any particular latitude. Even though powerful zonal jets on Jupiter are sometimes assumed to play a role of the barriers for the meridional mixing (e.g. [83]), Fig. 7 does not support this assumption. Instead, it demonstrates that the lateral dispersion is a Taylor diffusion process, both qualitatively and quantitatively, which is driven by macroturbulence with inverse

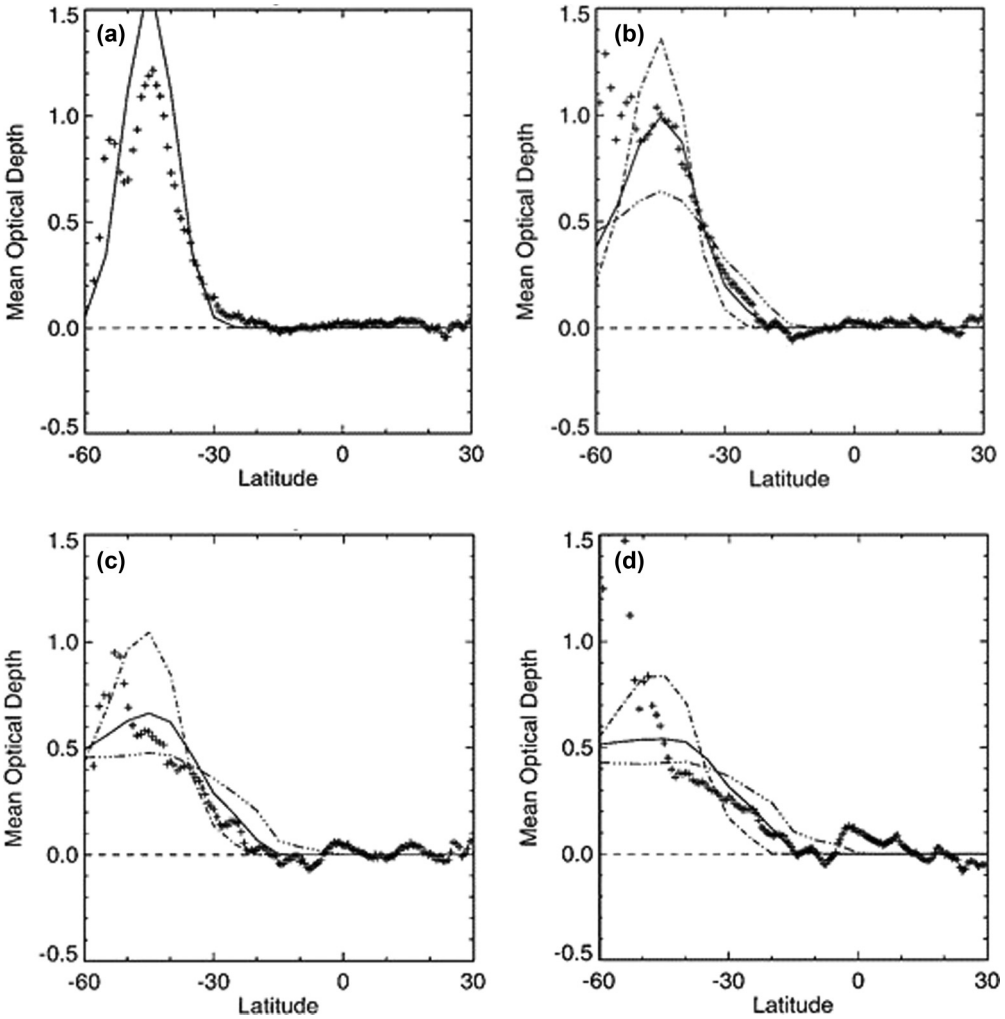

FIG. 7. Meridional spread of the debris following the collision of the Shoemaker-Levy 9 comet with Jupiter. The crosses represent longitude-mean perturbation optical depths at 230 nm derived from the changes in reflectivity after 18 May 1994: (a) 25 August 1994, (b) 4–5 March 1995, (c) 15 May 1996, and (d) 6 November 1997. Optical depths were integrated over longitude in each of the latitude bands between -60° and $+30^\circ$. Regions of negative mean optical depth are found where the average brightness of the bin was higher than it was prior to the arriving of impact debris. The solid lines are synthetic profiles calculated with the dynamical model that includes horizontal eddy diffusivity. Dash-dotted and dash-triple-dotted lines correspond to the results with the eddy diffusivity coefficient, respectively, reduced or increased by a factor of 5 compared to its nominal value. After Friedson *et al.* [27]; reprinted with the permission from Elsevier.

energy cascade. Note also that Figs. 6 and 7 demonstrate the affinity of the diffusion processes in vastly diverse flows that feature different regimes of anisotropic turbulence with opposite directions of the energy transfer and different types of dispersive waves.

Turning back to Eq. (20) we note that K_y depends on ϵ in both the Richardson's and Taylor's diffusion regimes, albeit in different fashions. The observation that the scale $\hat{L}_\beta$, delineating the transition between the two diffusion regimes, is intimately related to ϵ could be used to diagnose ϵ from diffusion observations. This new method could be employed as either an alternative or a supplement to the method of PV monotonizing. In practical applications, the transition scale can be estimated using the finite-scale Lyapunov exponent (FSLE) technique (e.g. [84]). The duality of the methods of estimating ϵ by PV monotonizing and a change in the diffusion regime will be elaborated in the following section using the previously employed experimental facility with a westward jet.

V. FSLE METHOD

Since the velocities in our experiments were estimated by tracking particle trajectories, we could use this information to evaluate particle dispersion with the FSLE technique. The FSLE quantifies an average growth rate of noninfinitesimal perturbations at different scales of observation [85]. Briefly, it is assumed that at time $t = 0$ a "reference" trajectory $\boldsymbol{x}(0)$ is perturbed to $\boldsymbol{x}'(0) = \boldsymbol{x}(0) + \delta\boldsymbol{x}(0)$, where $\|\delta\boldsymbol{x}(0)\| \equiv \delta_{\min} \ll 1$ (all length scales are nondimensionalized with the maximum characteristic length scale of the system). A sequence of thresholds δ_n, $n = 1, \ldots, N$, can be introduced with $\delta_n = \delta_1 \rho^{n-1}$, where the amplification factor is $\rho > 1$. Then, the statistics of the growth times $\tau(\delta)$ between δ and $\rho\delta$ is

computed on a large number of trajectory pairs, for each $\delta = \delta_n$. The FSLE is defined according to

$$\lambda(\delta) = \frac{\ln \rho}{\langle \tau(\delta) \rangle}, \tag{21}$$

where $\langle \tau(\delta) \rangle$ is the average time that the trajectory separation at scale δ takes to grow by a factor ρ (see also [86]). Different functional dependencies $\lambda = f(\delta_n)$ define different dispersion regimes (e.g. [39]).

FSLE can be a function of $\boldsymbol{x}$ in which case $\lambda(\delta,\boldsymbol{x})$ is a Lagrangian measure of the local amplification rate of a perturbation of size δ imposed on a trajectory initially passing through a point $\boldsymbol{x}$. In this case, Eq. (21) becomes

$$\lambda(\delta,\boldsymbol{x}) = \frac{1}{\langle \tau(\delta,\boldsymbol{x}) \rangle} \ln \rho, \tag{22}$$

which defines a map of the local rate of dispersion for an ensemble of trajectory pairs relative to their initial positions. We observe that for statistically stationary flows neither (21) nor (22) are explicitly time dependent. The FSLE maps diagnose regions with higher dispersion and those where dispersion is lower or null; the latter can be identified with the mixing barriers [87]. To account for anisotropic dispersion, the FSLE can be computed for the meridional and zonal components of the distance between particles separately as was done by Lacorata *et al.* [88] for dispersion in the lower stratosphere.

The initial dispersion is typically characterized by exponential growth of the fluid particles' separation. In this regime, relative dispersion is nonlocal and we expect $\lambda(\delta) \simeq \lambda_L = \text{const}$, λ_L being an estimate of the maximum Lagrangian Lyapunov exponent [84]. We identify the maximum separation of a particle pair attained at the end of the exponential regime as δ_L.

In flows with forcing, the initial, exponential stage of dispersion may evolve into the power law scaling $\lambda(\delta) \sim \delta^{-2/3}$ which corresponds to the Richardson's t^3 time dependence and Kolmogorov's (in 3D flows) or KK's (in 2D flows) $-5/3$ energy density spectrum. For either flow, the FSLE approach yields

$$\lambda(\delta) = \frac{C_R^{1/3} \ln \rho}{\rho^{2/3} - 1} \epsilon^{1/3} \delta^{-2/3}, \tag{23}$$

where $\delta > \delta_L$ and C_R is the Richardson constant. For 2D flows with inverse energy cascade, $C_R \sim O(1)$ [89]. The Richardson's law scaling may further evolve into the Taylor's diffusion regime for which $\lambda(\delta) \sim \delta^{-2}$. As mentioned earlier, in 2D turbulence with a β effect, the transition between the regimes is expected to occur at a geometrical scale $\delta_t \simeq \hat{L}_\beta$.

VI. TURBULENT DIFFUSION IN THE LABORATORY AND IMPLICATIONS FOR PLANETARY FLOWS

The three experiments analyzed in Sec. III were used for studies of the diffusion. The results are summarized in Figs. 8 and 9. The top row in Fig. 8 shows the FSLE maps, $\lambda(\delta,\boldsymbol{x})$, constructed by following two trajectories from an initial separation $\delta_0 = 0.7$ cm to a final separation threshold $\rho\delta$ over the observation time $T = 25$ s. The amplification factor is $\rho = 2$. If the final separation threshold was not attained after the time T, the FSLE was set to zero. The computed values were mapped onto trajectories' initial positions.

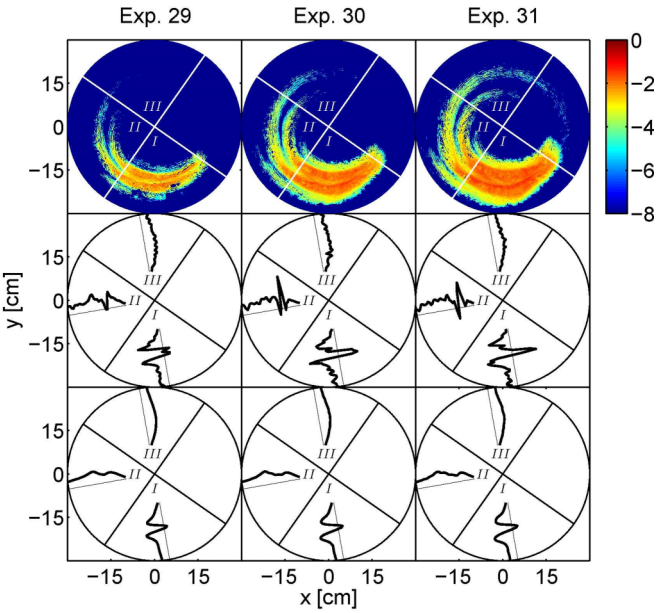

FIG. 8. FSLE maps (top), samples of instantaneous (middle), and fully time- and sector-averaged (bottom row) profiles of the radial PV gradient. The left, middle, and right columns pertain to the experiments 29, 30, and 31, respectively. The Roman numbers mark different sectors; sector I contains the magnets. While the flow in this sector is barotropically unstable most of the time, the occurrence of the instability decreases away from the sector. The color bar numbers show powers of 10.

The figure elucidates the differences in dispersion associated with forced and unforced jets. For the former, increasing turbulence intensity (measured by ϵ) enhances the dispersion. The increase in λ with increasing ϵ for a fixed δ is consistent with (23). One notes the FSLE decrease in the vicinity of the jet's axis and their asymmetry revealing somewhat larger dispersion on the "southern" flank of the jet. This asymmetry could be a result of the increase of the eddy size with increasing radius stipulated by the round geometry of the experimental device. While the FSLE is never null in the jet's domain over the forced sector I, it rapidly falls to zero around the middle part of the jet in the unforced sector II and is fully extinguished in sectors III and IV.

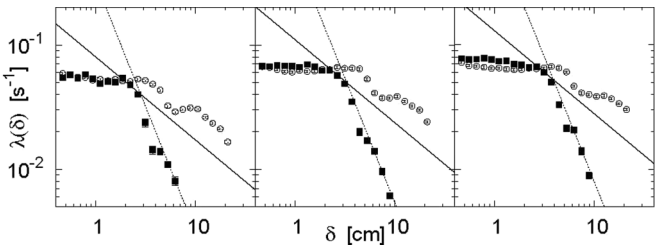

FIG. 9. Radial (black squares) and zonal (open circles) FSLE computed with $\rho = 2^{1/4}$. Straight lines represent the Richardson, $\lambda(\delta) \sim \delta^{-2/3}$ (solid), and Taylor, $\lambda(\delta) \sim \delta^{-2}$ (dotted), diffusion laws. Left, middle, and right panels pertain to the experiments 29, 30, and 31, respectively.

It was suggested in e.g. [83,90] that an unstable, easterly jet may become a mixing barrier and so our results in the unforced sectors do not appear surprising. It is not so in the forced sector I. Figure 2 in [83] and Fig. 3 in [90] indicate that easterly jets are associated with monotonic PV profiles thus implying that the jets' environs experienced no significant forcing due to the absence of the available rotational kinetic energy. In our experiments, however, forcing was applied to sector I and the ensuing turbulence played a major role in the dynamics and dispersion. Figure 8 shows persistent instability in sector I, while Fig. 3 shows that the instabilities were migrating between the "northern" and "southern" flanks of the jet and could be aligned with the locations of FSLE maxima. The instability sporadically occurs in sector II even though the flow there is not forced directly. In sector III, the flow is practically always stable, although some residual turbulence might survive.

The rapid decrease of λ along the central section of the jet in sectors II and III can be explained by the absence of the direct forcing and is somewhat reminiscent of the manifestation of a mixing barrier in the easterly jet as elaborated in [83,90]. A slower decay of λ on the jet's flanks over the unforced sectors can probably be attributed to the remote forcing by the breaking Rossby waves as they propagate westward from sector I. A weak forcing in sector II leads to a collapse of the radial dispersion while most of the zonal dispersion appears to be due to the advection by the jet.

In summary, forced westward jets do not act as mixing barriers due to nonzero cross-jet turbulent diffusion. The enhanced mixing on jets' flanks can be facilitated by turbulence developing from the barotropic instability. These conclusions are in line with the results discussed in Sec. IV regarding the Jovian zonal jets. It was argued, and also elucidated by Fig. 7, that, however powerful, the jets cannot suppress meridional diffusion which is sustained by macroturbulence. The magnitude of the meridional diffusivity coefficient in the Taylor's regime can be estimated from Eq. (20) and is consistent with the values inferred from observations.

Further insight into diffusion by macroturbulence is provided by the FSLE analysis of the experimental results summarized in Fig. 9 and Table II. By showing the FSLEs in the radial (meridional) and azimuthal (zonal) directions, Fig. 9 underscores the anisotropic nature of dispersion in turbulence with a β effect. In all three experiments, the zonal FSLEs display two successive plateaus. As the FSLE plateaus correspond to the exponential dispersion of two Lagrangian particles trapped in a coherent structure (e.g. [85]), one can identify the first plateau with single eddies on both sides of the jet, and the second one with the entire zonal meandering "ribbon." Thus the two major scales corresponding to these structures are the size of the eddies estimated at about 5–6 cm, and the wavelength of the ribbon, about 20 cm. Subsequently, the first zonal plateau ends at about 5–6 cm followed, after a short transition, by a lower secondary plateau extending to about 20 cm. At its exit, the zonal FSLEs have a slope compatible with the Richardson's regime. This regime could be anticipated because the Rossby wave elasticity that facilitates the Richardson-Taylor regime transition in the radial direction does not act in the zonal direction. The secondary plateau being lower reflects the decrease in the dispersion rate caused by a temporary "trapping" of the Lagrangian particles by the meandering ribbon inside of which the particles can recirculate while departing from each other. This does not occur, of course, when the separation is smaller than the size of a single eddy, and this is why the separation in that case is somewhat faster.

TABLE II. Comparison of the scale $\hat{L}_\beta$ with the transitional scale δ_T and PV monotonizing scale L_M.

Expt.	$\hat{L}_\beta$ (cm)	δ_T (cm)	L_M (cm)	$\hat{L}_\beta/L_M$
29	2.5	2.6	1.3	1.9
30	3.4	3.1	1.7	2.0
31	3.7	3.8	1.9	1.95

Bounded by the Rossby wave elasticity, there are no secondary structures in the radial direction and so the radial FSLEs have only one plateau. As $\delta \to 0$, the FSLE levels in the radial and zonal directions are approximately equal because in this limit, the dispersion is isotropic. Since the zonal plateau accounts for the translation of eddies in the zonal direction, it is always somewhat longer than its meridional counterpart. At the exit from the meridional plateau, denoted δ_L, the FSLE exhibits a short range of the Richardson's regime at the end of which, denoted δ_T and computed in excess of δ_L, it experiences sharp crossover to the Taylor's regime. As evident from Table II, the range of the Richardson's regime, δ_T, is very close to the measured values of $\hat{L}_\beta$. In addition, one observes a nearly constant ratio between $\hat{L}_\beta$ and L_M, $\hat{L}_\beta/L_M \simeq 2$. These results point to the affinity between the Richardson's diffusion regime and PV mixing as both are powered by the Kolmogorov-Kraichnan turbulence. The constant ratio of $\hat{L}_\beta$ and L_M ensures consistency between the estimates of ϵ from the kinetic energy spectra, PV monotonizing, and meridional dispersion.

VII. DISCUSSION AND CONCLUSIONS

The application of the results of this investigation to the analysis of dispersion processes on Jupiter and, possibly, other gas giant planets was discussed in Sec. IV. In the oceanographic context, these results are even more useful because more dispersion data is available.

Studies by, e.g., LaCasce and Bower [23], Ollitrault *et al.* [91], LaCasce [25], Lumpkin and Elipot [26] indicate that Richardson's and Taylor's diffusion regimes are ubiquitous in the World ocean. The transition between the regimes in the subsurface layer occurs on scales of 200–300 km which are of the order of the width of the alternating zonal jets [3,66]. Several investigations note strong diffusion anisotropy (e.g. [92–94]), whereas meridional diffusivities are much smaller than their zonal counterparts. Diffusion anisotropization is sometimes attributed to the effect of the mean zonal flow upon the lateral diffusivity [95]. The present results point to an alternative explanation of this phenomenon, i.e., the anisotropization of the inverse energy cascade at the crossover length scale $\hat{L}_\beta$. The oceanic kinetic energy spectra usually deviate from the

KK and zonostrophic distributions and so the coefficient in (8) is prone to some uncertainty. In addition, this coefficient may vary with geographic location. Using (8) and taking $\beta \sim 10^{-11}$ m^{-1} s^{-1} and $L \sim 200$–300 km, one evaluates ϵ between 10^{-8} and 10^{-9} m^2 s^{-3}, which is not dissimilar to the values reported by Arbic *et al.* [96]. According to (20), such ϵ yields K_y in the range between 2.5×10^3 and 10^4 m^2 s^{-1}, also in agreement with the observed values (e.g. [92–94]).

For the deep water, LaCasce and Bower [23] show the transition at $L \sim 100$ km, which gives $\epsilon \sim 10^{-10}$ m^2 s^{-3}, in quantitative agreement with the estimates found in e.g. [3,97]. Then, K_y is evaluated at about 10^3 m^2 s^{-1}. The decrease of ϵ with depth is consistent with the decrease of the eddy kinetic energy [94] and stems from the differences in energy partitioning among the modes. The surface signal reflects inverse cascade in the baroclinic mode which is more energetic than its counterpart in the deep ocean which is mostly barotropic [98].

Concluding we reemphasize that a combination of PV monotonizing and particles' dispersion characteristics offers a powerful and effective tool for quantification of macroturbulence. This tool has predictive skills and offers a plethora of applications in studies of planetary circulations as well as the large-scale oceanic circulations and climate.

ACKNOWLEDGMENTS

The authors are grateful to Peter Read, James Cho, Igor Kamenkovich, Roland Young, and Victor Shrira for fruitful discussions that helped to improve the manuscript. Reviewers' comments aided in manuscript's clarification. Jim Ledwell and Jim Friedson made Figs. 6 and 7 available to us. B.G. and J.H. gratefully acknowledge partial support by ARO Grant No. W911NF-09-1-0018 and ONR Grant No. N00014-07-1-1065. G.L. thanks Research Programs "SSD PESCA" and "RITMARE" for providing financial support.

[1] A. Sánchez-Lavega, *An Introduction to Planetary Atmospheres* (CRC Press, Boca Raton, FL, 2011).
[2] J. Pedlosky, *Ocean Circulation Theory*, 2nd ed. (Springer, New York, 1998).
[3] B. Galperin, H. Nakano, H.-P. Huang, and S. Sukoriansky, Geophys. Res. Lett. **31**, L13303 (2004).
[4] A. Davis, E. Di Lorenzo, H. Luo, A. Belmadani, N. Maximenko, O. Melnichenko, and N. Schneider, Geophys. Res. Lett. **41**, 948 (2014).
[5] C. Buckingham, P. Cornillon, F. Schloesser, and K. Obenour, J. Geophys. Res. Oceans **119**, 4840 (2014).
[6] M. Baldwin, P. Rhines, H.-P. Huang, and M. McIntyre, Science **315**, 467 (2007).
[7] J. Pedlosky, *Geophysical Fluid Dynamics*, 2nd ed. (Springer-Verlag, Berlin, 1987).
[8] M. McIntyre, Adv. Geosci. **15**, 47 (2008).
[9] B. Galperin, S. Sukoriansky, and N. Dikovskaya, Ocean Dyn. **60**, 427 (2010).
[10] I. Held, Tellus A **51**, 59 (1999).
[11] O. M. Phillips, Deep-Sea Res. **19**, 79 (1972).
[12] O. Phillips, *The Dynamics of the Upper Ocean*, 2nd ed. (Cambridge University Press, Cambridge, UK, 1977).
[13] S. Thorpe, Philos. Trans. R. Soc. London A **286**, 125 (1977).
[14] S. Thorpe, Annu. Rev. Earth Planet. Sci. **32**, 91 (2004).
[15] S. Thorpe, *The Turbulent Ocean* (Cambridge University Press, Cambridge, UK, 2005).
[16] B. Galperin, J. Hoemann, S. Espa, and G. Di Nitto, Geophys. Res. Lett. **41**, 6237 (2014).
[17] E. N. Pelinovsky, Oceanology **18**, 126 (1978).
[18] G. Vallis and M. Maltrud, J. Phys. Oceanogr. **23**, 1346 (1993).
[19] A. Chekhlov, S. Orszag, S. Sukoriansky, B. Galperin, and I. Staroselsky, Physica D **98**, 321 (1996).
[20] Note that a scale L_β discussed in, e.g., Ref. [9] was larger than the present definition by about a factor of 2. To avoid the confusion, that scale will be denoted here as $\hat{L}_\beta$; it will be introduced later. All the criteria derived in [9] will be modified accordingly.
[21] S. Sukoriansky, B. Galperin, and I. Staroselsky, Phys. Fluids **17**, 085107 (2005).
[22] S. Sukoriansky and B. Galperin, J. Fluid Mech. **805**, 384 (2016).
[23] J. H. LaCasce and A. Bower, J. Mar. Res. **58**, 863 (2000).
[24] C. Garrett, Prog. Oceanogr. **70**, 113 (2006).
[25] J. LaCasce, Prog. Oceanogr. **88**, 1 (2008).
[26] R. Lumpkin and S. Elipot, J. Geophys. Res. **115**, C12017 (2010).
[27] A. Friedson, R. West, A. Hronek, N. Larsen, and N. Dalal, Icarus **138**, 141 (1999).
[28] B. Galperin, R. Young, S. Sukoriansky, N. Dikovskaya, P. Read, A. Lancaster, and D. Armstrong, Icarus **229**, 295 (2014).
[29] S. Sukoriansky, N. Dikovskaya, and B. Galperin, Geophys. Res. Lett. **36**, L14609 (2009).
[30] D. Dritschel and M. McIntyre, J. Atmos. Sci. **65**, 855 (2008).
[31] R. Weisberg and T. Weingartner, J. Phys. Oceanogr. **18**, 1641 (1988).
[32] D. Chelton, F. Wentz, C. Genremann, R. de Szoeke, and M. Schlax, Geophys. Res. Lett. **27**, 1239 (2000).
[33] J. Farrar, J. Phys. Oceanogr. **41**, 1160 (2011).
[34] J.-Y. Yu and W. Liu, Geophys. Res. Lett. **30**, 1735 (2003).
[35] A. Ingersoll and D. Pollard, Icarus **52**, 62 (1982).
[36] R. Cosentino, A. Simon, R. Morales-Juberias, and K. Sayanagi, Astrophys. J. Lett. **810**, 10 (2015).
[37] D. S. Choi, A. P. Showman, and R. H. Brown, J. Geophys. Res. **114**, E04007 (2009).
[38] K. Sayanagi, U. Dyudina, S. Ewald, G. Muro, and A. Ingersoll, Icarus **229**, 170 (2014).
[39] G. Lacorata and S. Espa, Geophys. Res. Lett. **39**, L11605 (2012).
[40] S. Espa, G. Lacorata, and G. Di Nitto, J. Phys. Oceanogr. **44**, 632 (2014).
[41] G. Vallis, *Atmospheric and Oceanic Fluid Dynamics* (Cambridge University Press, Cambridge, UK, 2006).
[42] P. Rhines, J. Fluid Mech. **69**, 417 (1975).
[43] P. Rhines, Chaos **4**, 313 (1994).
[44] B. Galperin, S. Sukoriansky, N. Dikovskaya, P. Read, Y. Yamazaki, and R. Wordsworth, Nonlin. Proc. Geophys. **13**, 83 (2006).

[45] Y. Afanasyev and J. Wells, Geophys. Astrophys. Fluid Dyn. **99**, 1 (2005).
[46] S. Sukoriansky, N. Dikovskaya, R. Grimshaw, and B. Galperin, in *Rossby Waves and Zonons in Zonostrophic Turbulence*, AIP Conf. Proc. No. 1439 (American Institute of Physics, Melville, NY, 2012), pp. 111–122.
[47] D. Chelton, M. Schlax, and R. Samelson, Prog. Oceanogr. **91**, 167 (2011).
[48] J. Sommeria, S. Meyers, and H. Swinney, in *Nonlinear Topics in Ocean Physics*, edited by A. Osborne (North-Holland, Amsterdam, 1991), pp. 227–269.
[49] J. Aubert, S. Jung, and H. Swinney, Geophys. Res. Lett. **29**, 1876 (2002).
[50] G. Arfken, H. Weber, and F. Harris, *Mathematical Methods for Physicists*, seventh ed. (Elsevier-AP, Amsterdam, 2013).
[51] The log-log representation using n is approximately correct since α_{mn} is approximately proportional to n for all m. The coefficient is about 3 for $m = 0$ and gradually increases with m and n.
[52] U. Frisch, *Turbulence, the Legacy of A.N. Kolmogorov* (Cambridge University Press, Cambridge, UK, 1995), p. 296.
[53] E. Lindborg, J. Fluid Mech. **388**, 259 (1999).
[54] G. Boffetta and S. Musacchio, Phys. Rev. E **82**, 016307 (2010).
[55] G. Boffetta and R. Ecke, Annu. Rev. Fluid Mech. **44**, 427 (2012).
[56] G. King, J. Vogelzang, and A. Stoffelen, J. Geophys. Res. Oceans **120**, 346 (2015).
[57] E. Lindborg and J. Cho, J. Geophys. Res. **106**, 10233 (2001).
[58] E. Lindborg, J. Fluid Mech. **572**, 255 (2007).
[59] L. Biferale and I. Procaccia, Phys. Rep. **414**, 43 (2005).
[60] H.-P. Huang, B. Galperin, and S. Sukoriansky, Phys. Fluids **13**, 225 (2001).
[61] S. Sukoriansky, N. Dikovskaya, and B. Galperin, J. Atmos. Sci. **64**, 3312 (2007).
[62] A. Okuno and A. Masuda, Phys. Fluids **15**, 56 (2003).
[63] I. Kamenkovich, P. Berloff, and J. Pedlosky, J. Phys. Oceanogr. **39**, 1361 (2009).
[64] P. Berloff, S. Karabasov, T. Farrar, and I. Kamenkovich, J. Fluid Mech. **686**, 534 (2011).
[65] D. B. Chelton, M. G. Schlax, R. M. Samelson, and R. A. de Szoeke, Geophys. Res. Lett. **34**, L15606 (2007).
[66] N. Maximenko, B. Bang, and H. Sasaki, Geophys. Res. Lett. **32**, L12607 (2005).
[67] B. Galperin, S. Sukoriansky, and N. Dikovskaya, Phys. Scr. **T132**, 014034 (2008).
[68] G. I. Taylor, Proc. London Math. Soc. **s2-20**, 196 (1922).
[69] G. Mellor and T. Yamada, Rev. Geophys. Space Phys. **20**, 851 (1982).
[70] C. Garrett, J. Geophys. Res. **94**, 9710 (1989).
[71] F. Bretherton, Quart. J. R. Meteor. Soc. **92**, 325 (1966).
[72] J. Green, Quart. J. Roy. Meteor. Soc. **96**, 157 (1970).
[73] I. Held and V. Larichev, J. Atmos. Sci. **53**, 946 (1996).
[74] M. Visbeck, J. Marshall, and T. Haine, J. Phys. Oceanogr. **27**, 381 (1997).
[75] C. Eden and R. Greatbatch, Ocean Modell. **20**, 223 (2008).
[76] D. Marshall and A. Adcroft, Ocean Modell. **32**, 188 (2010).
[77] A. Klocker and R. Abernathey, J. Phys. Oceanogr. **44**, 1030 (2013).
[78] L. Richardson, Proc. R. Soc. London. Ser. A **110**, 709 (1926).
[79] B. Galperin and S. Sukoriansky, Ocean Dyn. **60**, 1319 (2010).
[80] B. Galperin, S. Sukoriansky, and H.-P. Huang, Phys. Fluids **13**, 1545 (2001).
[81] J. Ledwell, L. Laurent, J. Girton, and J. Toole, J. Phys. Oceanogr. **41**, 241 (2011).
[82] J. Harrington, I. de Pater, S. Brecht, D. Deming, V. Meadows, and P. Nicholson, in *Jupiter: The Planet, Satellites, and Magnetosphere*, edited by F. Bagenal, T. Dowling, and W. McKinnon (Cambridge University Press, Cambridge, UK, 2004), pp. 159–184.
[83] F. Beron-Vera, M. Brown, M. Olascoaga, I. Rypina, H. Koçak, and I. Udovydchenkov, J. Atmos. Sci. **65**, 3316 (2008).
[84] T. Bohr, M. Jensen, G. Paladin, and A. Vulpiani, *Dynamical Systems Approach to Turbulence* (Cambridge University Press, Cambridge, UK, 1998), p. 350.
[85] M. Cencini and A. Vulpiani, J. Phys. A: Math. Theor. **46**, 254019 (2013).
[86] G. Boffetta and A. Celani, Physica A **280**, 1 (2000).
[87] G. Boffetta, G. Lacorata, G. Redaelli, and A. Vulpiani, Physica D **159**, 58 (2001).
[88] G. Lacorata, E. Aurell, B. Legras, and A. Vulpiani, J. Atmos. Sci. **61**, 2936 (2004).
[89] G. Boffetta and I. Sokolov, Phys. Fluids **14**, 3224 (2002).
[90] F. Beron-Vera, M. Olascoaga, M. Brown, and H. Koçak, J. Atmos. Sci. **69**, 753 (2012).
[91] M. Ollitrault, C. Gabillet, and A. Colin de Verdiére, J. Fluid Mech. **533**, 381 (2005).
[92] V. Zhurbas and I. Oh, J. Geophys. Res. **108**, 3141 (2003).
[93] V. Zhurbas and I. S. Oh, J. Geophys. Res. **109**, C05015 (2004).
[94] S. Chiswell, J. Phys. Oceanogr. **43**, 2718 (2013).
[95] R. Ferrari and M. Nikurashin, J. Phys. Oceanogr. **40**, 1501 (2010).
[96] B. Arbic, M. Müller, J. Richman, J. Shriver, A. Morten, R. Scott, G. Sérazin, and T. Penduff, J. Phys. Oceanogr. **44**, 2050 (2014).
[97] M. Ollitrault, M. Lankhorst, D. Fratantoni, P. Richardson, and W. Zenk, Geophys. Res. Lett. **33**, L05605 (2006).
[98] C. Wunsch, J. Phys. Oceanogr. **27**, 1770 (1997).